Magnetic Power Distribution Using Controlled Permeability Bypass and Its Multiple Output Investigation

Teke Hua, *Student Member, IEEE*, Manxin Chen, *Student Member, IEEE*, and Ka Wai Eric Cheng, *Fellow, IEEE*

***Abstract*—An alternative wireless power transfer (WPT) using near-field magnetic power distribution is proposed. The new method is characterized by using a low permeability path in serial with a high permeability path as the main unit or the basic cell. The output can be tapped into the main unit by paralleling the low permeability path. The magnetic cores are integrated with different permeability to form a multiple-transmitter geometry. Every transmitter corresponds to more than one receiver that is integrated with back-end circuits such as rectifiers to convert ac voltage into dc voltage. The receiver can be easily installed in the electrical devices, and hence power is transferred wirelessly to drive the devices. Analysis of the working mechanisms of the proposed WPT system is given in detail and design considerations are also investigated. Power loss distributions for the converter and coupler are also analyzed fully. Experimental results show that a basic cell driven by an 80 kHz pulse wave, supplying three resistive loads at 321 W achieves 86.6% efficiency. The system efficiency can be maintained at a high level over a wide output power range. Finally, a magnetic panel comprising seven basic cells supplying multiple loads is demonstrated. Results show the feasibility of the proposed system by lighting up multiple LED loads.**

***Index Terms*—Magnetic cores, magnetic coupling coefficient, magnetic platform, magnetic power distribution, multiple outputs, wireless power transfer (WPT).**

I. Introduction

DUE to the unique advantages of wireless power transfer (WPT) including flexibility, safety and improved user experience, this technique has attracted more and more attention. The WPT is based on magnetic coupling and is now the recent method of power transfer without direct electrical contact. It is also significantly reported in the last few years [1], [2], [3], [4], [5], [6], [7], [8], [9], [10]. The research objective is certainly focused on a higher power and higher efficiency. A simple WPT system is using a single transmitter with a resonant network. The coupling may not be high especially when the magnetic core is not employed [1], [2], [3]. In order to increase the power transfer, a high magnetic current, and field must be generated that may occur high power loss in the winding. The power transfer performance of the WPT system is significantly influenced by the level of coupling between the primary and secondary windings. Higher levels of magnetizing current increase the loss in these systems, resulting in lower efficiency. A single transmitter and received set are of a common arrangement but the efficiency is not optimal [4]. An alternative design using multiple transmitters has been reported in [5], [6], [7], and [8]. Compared to the single transmitter, implementing multiple transmitters in a WPT system has been shown to enhance power transfer capability and transfer efficiency [7], [8]. Air core-based WPT system is an issue because the leakage flux cannot be controlled well and it reduces the coupling coefficient. The fragility and leakage fields deteriorate the coupling from the primary side to the secondary side. For this problem, a network that behaves as a resonant conversion can be used to compensate for the leakage flux to reduce the loss of the magnetizing current. Improvements in conversion have been found [9], [10], [11], but the circuit becomes more complex.

Unlike coreless WPT systems, high-permeability magnetic cores have been shown to exhibit a higher coupling coefficient [12], [13], [14]. This is due to the fact that the high permeability core can also reduce the reluctance and thus the eddy current loss [15], [16], [17], [18], [19]. But there are also disadvantages. One of the main concerns is the bulky size of the magnetic core, which would make it less attractive to some applications such as movable electronics chargers. Nonetheless, it remains a viable option for larger electrical devices such as in-house electrical equipment or WPT platform.

The study here examines a new type of WPT cell that allows multiple transmitters and multiple receivers. It is aimed to provide a new, simple and flexible wireless magnetic power distribution method in large areas such as residential and offices as an alternative to wired power distribution, which can eliminate some problems of wired power distribution, such as aging or electric leakage. These proposed cells can be installed in a wall

Manuscript received 15 March 2023; revised 13 May 2023 and 2 July 2023; accepted 2 August 2023. Date of publication 7 August 2023; date of current version 22 September 2023. This work was supported by UGC Research Grants Council GRF Hong Kong under Grant PolyU152218/19E. Recommended for publication by Associate Editor J. Acero. *(Corresponding author: Ka Wai Eric Cheng.)*

Teke Hua and Ka Wai Eric Cheng are with the Electrical and Electronic Engineering, The Hong Kong Polytechnic University, Hong Kong (e-mail: tekeee.hua@connect.polyu.hk; eeecheng@polyu.edu.hk).

Manxin Chen is with the Chinese University of Hong Kong, Hong Kong (e-mail: mxchen@link.cuhk.edu.hk).

Color versions of one or more figures in this article are available at https://doi.org/10.1109/TPEL.2023.3302619.

Digital Object Identifier 10.1109/TPEL.2023.3302619

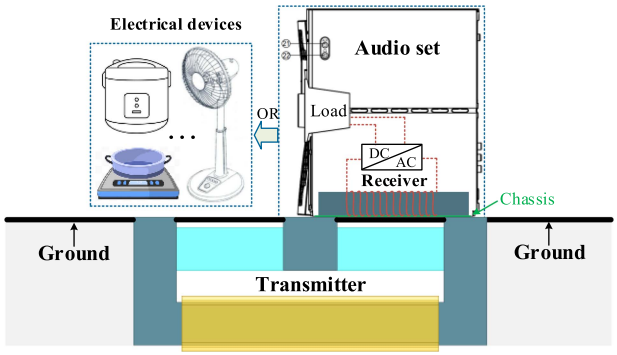

Fig. 1. Application of the proposed system driving an electrical device.

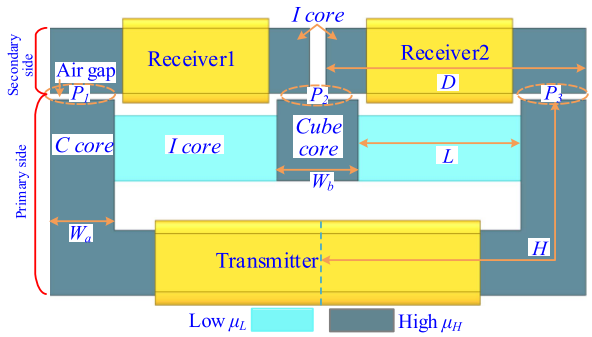

Fig. 2. Basic cell with two transmitters and receivers.

or ground where in-house devices are erected. By integrating a secondary core in these devices such as TV sets, audio sets, rice cookers, or induction cookers, power is therefore transferred without any cables connected. Taking the audio set as an example, the schematic diagram of the device installation is shown in Fig. 1. However, for the devices, such as rice cookers or induction cookers, the transmitter can be installed on the kitchen worktop. Therefore, the use of WPT cells also makes residents or offices become "socket-less" for people to live in, reducing the chances of electrical shock. Since the output is ac voltage, power electronics circuits such as rectifiers with suitable control strategy [20], [21] and dc converters [22], [23] are recommended to serve as intermediaries between the output of the WPT system and targeted devices. The proposed basic cells for the WPT system incorporate high-permeability magnetic cores, which ensures that the proposed basic structure can provide a good coupling coefficient between the transmitter and receiver when the basic structure is extended to a single-input multiple-output system regardless of the location and the size of the transmitter. The receivers can be coupled to the transmitter by simply tapping to the flux path in a region via the connection of magnetic cores. For the coreless WPT system, the receivers must be limited within the dimension of the transmitter coil when realizing the multiple-output structure [24], which restricts the application of the coreless WPT system to provide multiple outputs in a large area situation. Therefore, the proposed work can significantly simplify the power transfer process and increase power transfer efficiency in a flexible and simple manner. The analysis of the proposed basic cell is provided in-depth, and a theoretical power loss distribution of the proposed near-field WPT system is derived in detail.

The article is to present the investigation of a magnetic distribution WPT method for supplying in-house electrical devices that are positioned in close proximity to the ground or panels. Compared with the previous publications, the contribution of this article is to provide a possible solution for determining the power transfer efficiency through the coupling coefficient. Consequently, an initial selection of the permeability of the magnetic core enables the estimation of the power transfer efficiency of the system.

The rest of this article is organized as follows. Section II outlines the proposed coupling structure. In Section III, the three connection mechanism conditions with two receivers are analyzed in detail, with a particular focus on the magnetic reluctance models. The implementation of the magnetic wall system, which generalizes the basic cell, is presented in Section IV. Design considerations for the proposed basic cell, along with loss analysis, are discussed in detail in Section V. In Section VI a detailed comparison with the traditional method is performed. Section VII presents experimental results. Finally, Section VIII concludes this article.

II. Proposed Coupling Structure

Fig. 2 shows the proposed magnetic coupling structure of the WPT system. The primary side is made up of two types of magnetic cores, which has high permeability (denoted as μ_H) and low permeability (denoted as μ_L), where the high or low permeability used below is referred to as the relative permeability to facilitate the discussion. It can be seen as a *C core* of high permeability and two *I cores* of low permeability with a high permeability *cube core* segregated in between. The secondary side cores are also of high permeability. Firstly, the cross-section of the *C core* used in the article is proposed to be square

$$A_e = W_a \times W_a \tag{1}$$

where w_a is the core width. For simplifying the study, all the *I cores* used in the article are designed to be the same cross-sectional area and are named *C core*, and the width of the *cube core* is w_b and is greater than w_a ($w_b > w_a$). *L* is the low permeability fixed path length of the *I core* with low permeability, while *D* is the high permeability receiver path length of *I core* with high magnetic permeability. *H* is half of the equivalent magnetic path length of the *C core*.

To generate a stable magnetic field, an ac voltage source is required to be connected to the primary side. There are three poles of the primary side available for getting power, named P_1, P_2 (the *cube core*), and P_3. Two magnetic cores with μ_H across P_1 and P_2, or P_2 and P_3 can serve as secondary side receivers and the output can be connected to loads. To produce a constant dc voltage at the output, rectifiers and dc converters are recommended. All the components, including the secondary side magnetic cores, can be installed inside a targeted device. When the device is turned ON, it can simply be moved to panels where there are basic cells of the proposed system.

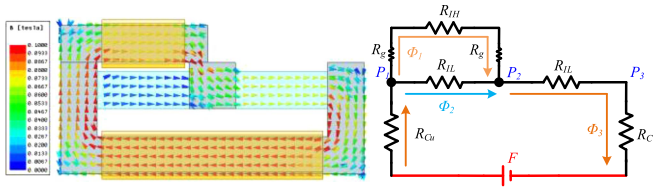

Fig. 3. Single-receiver mechanism and its magnetic model.

III. Working Mechanism of the Proposed Basic Cell

The construction of the basic cell of three operation mechanisms and its associated magnetic reluctance model are analyzed in this section. Since there are cores with different permeability on the primary side, the magnetic path will be adjusted by varying the placement of the receivers. The placement mechanisms of operation are outlined as follows.

1) *Single Receiver Mechanism:* Only one secondary-side core taps the output and the main flux is channeled to the secondary-side core.
2) *Two-Receiver Mechanism:* Two secondary-side cores are tapped to two outputs. The main flux is mostly channeled to the secondary-side cores and converts to two outputs.
3) *No Receiver Mechanism:* No secondary-side core is used. The basic cell then behaves as a simple inductor.

The basic cell is formed by two lower permeability *I cores*. It should be noted that with more than two transmitters and multiple receivers, there will be more than three working mechanisms for every basic cell. However, the flux paths of multiple transmitters and multiple receivers can be derived from this basic cell. Without loss of generality and to conduct an idealized analysis, the following assumption is made.

1) μ_H is high enough ($\mu_H \gg \mu_L$). The leakage flux near the core with μ_H in the air is so small that it can be ignored.
2) The connection of the primary side is ideal, i.e., the air gaps are neglected.
3) Magnetic cores are not saturated.

A. Single-Receiver Mechanism

In this mechanism, a single *I core* with permeability μ_H is placed on the secondary side as a receiver for the output. The magnetic fluxes of the main path through the input transmitter, bypass receiver path and low permeability *I core* path magnetic flux is illustrated in Fig. 3, Reluctance of with high permeability μ_H can be expressed as

$$R_{IH} = \frac{D}{\mu_H A_e \mu_0} \tag{2}$$

$$R_{TC} = R_{Cu} + R_C = \frac{2H + W_b}{\mu_H A_e \mu_0} \tag{3}$$

where R_I is the reluctance of receiver *I core*, and R_{TC} is the equivalent reluctance of the *C core* and *Cube core*.

Likewise, the reluctance of *I core* is relatively high because it is formed by the low permeability u_L

$$R_{u_L} = \frac{L}{\mu_L A_e \mu_0} \tag{4}$$

where R_g is the reluctance of air gaps between the primary side and secondary side which can be represented as

$$R_g = \frac{l_g}{A_e u_0} \tag{5}$$

where l_g represents the air connection displacement between primary and secondary cores, which corresponds to the thickness of the device's package in practical applications.

As shown in Fig. 3, let the magnetomotive force (mmf) be F, thus the coupling coefficient k is

$$k = \frac{\emptyset_1}{\emptyset_1 + \emptyset_2} \tag{6}$$

where

$$\emptyset_1 = \frac{F}{[(2R_g + R_{IH})//R_{IL} + R_{IL} + R_{TC}]} \times \frac{(R_{IH} + 2R_g)//R_{IL}}{R_{IH} + 2R_g} \tag{7}$$

$$\emptyset_2 = \frac{F}{[(2R_g + R_{IH})//R_{IL} + R_{IL} + R_{TC}]} \times \frac{(R_{IH} + 2R_g)//R_{IL}}{R_{IL}}. \tag{8}$$

It follows that, k can be simplified as

$$k = \frac{\frac{F}{[(2R_g+R_{IH})//R_{IL}+R_{IL}+R_{TC}]} \times \frac{(R_{IH}+2R_g)//R_{IL}}{R_{IH}+2R_g}}{\frac{F(R_{IH}+2R_g)//R_{IL}}{[(2R_g+R_{IH})//R_{IL}+R_{IL}+R_{TC}]} \times \left(\frac{1}{R_{IH}+2R_g} + \frac{1}{R_{IL}}\right)} \tag{9}$$

where $R_{IL} = R_{\mu_L}$, because both *I cores* are designed with the same shape and the same length and the same permeability μ_L.

Hence, the coupling coefficient expression is further reduced from (9) to

$$k = \frac{1}{1 + \frac{R_{IH}+2R_g}{R_{IL}}}. \tag{10}$$

The coupling coefficient is characterized by high- and low-permeability magnetic reluctance and air gap reluctance. R_g is determined by the gap length which is fixed after the geometrical shape is established. The coupling efficiency is only adjusted by varying R_{IL}. That is to say, μ_L determines k. More, intuitively, the relationship between coupling coefficient k and the relative permeability μ_L can be depicted in Fig. 4, when $W_a = 20$ mm, $W_b = 25$ mm, $D = 80$ mm, $L = 60$ mm, $H = 122.5$ mm, and $l_g = 2.5$ mm, 3.5 mm and 4.5 mm.

It indicates in Fig. 4 that the larger relative permeability μ_L, the smaller coupling coefficient k. Because an increase in the relative permeability μ_L leads to a decrease in the reluctance of low-permeability *I core,* according to (4). Thus, it can conduct more magnetic flux, which, in turn, causes a decrease in the magnetic flux density of the high-permeability *I core* in the secondary side. If the relative permeability μ_L is increased to be the same as μ_H, it will be able to conduct the majority of magnetic flux, since the high permeability μ_H is several thousand times greater than the permeability of air, i.e., $R_{IH} \ll R_g$, so that the coupling coefficient k will be reduced to close to zero, as shown in (11) and Fig. 5(a).

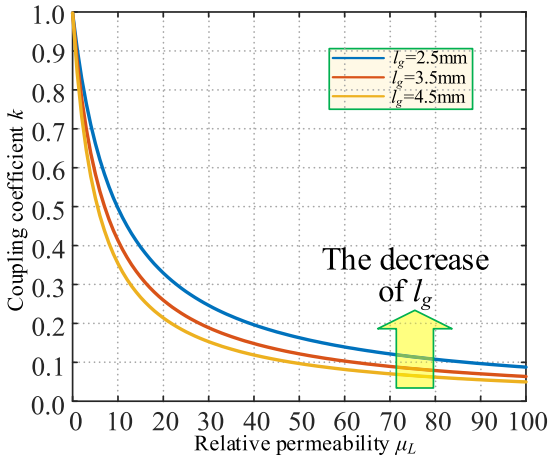

Fig. 4. Coupling coefficient of the one-receiver mechanism with different R_g.

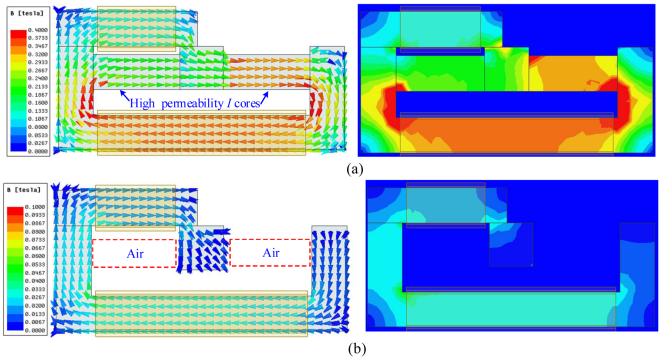

Fig. 5. Simulation results of magnetic flux vector and magnetic field distribution. (a) High-permeability core employed in the transmitter. (b) Air employed in the transmitter.

In addition, the smaller relative permeability μ_L, the larger coupling coefficient k in theory, according to Fig. 4. However, if the low-permeability *I core* is directly replaced with the air, as illustrated in Fig. 5(b), effective coupling between the transmitter and receiver is not formed due to the lack of low-permeability *I cores* to confine the magnetic flux. Thus, no effective flux loop will be established in the single-receiver mechanism. Therefore, low-permeability cores are the most suitable option to be integrated into the transmitter. Moreover, the coupling coefficient k decreases when the air gap length l_g between the primary side and the secondary side becomes larger. Therefore, the air gap length can be regulated according to the actual process requirement

$$k = \frac{1}{2 + \frac{2R_g}{R_H}}. \tag{11}$$

B. Two-Receiver Mechanism

Under this mechanism, where two μ_H cores serve as receivers and are behaving as the transformer's secondary sides, the magnetic fluxes of the main path through the transmitter, two bypass loads in the loads and the low permeability path of the are shown in Fig. 6. Compared with the one-receiver mechanism, the magnetic flux density in the two-receiver mechanism is higher

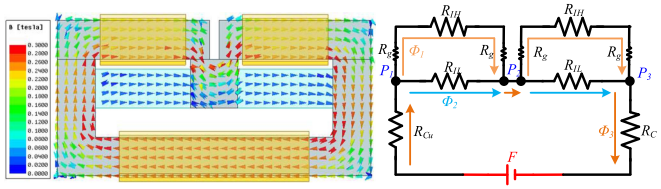

Fig. 6. Two-load mechanism and its magnetic model.

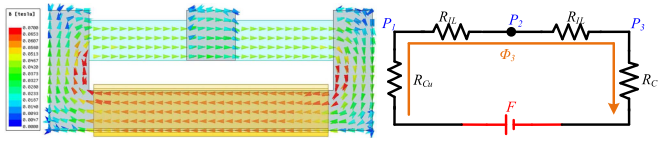

Fig. 7. No-load mechanism and its magnetic model.

owing to the fact that the low-permeability L core is bypassed by the high-permeability L core. In this configuration, there are two coupling coefficients, denoted as k_1 and k_2, corresponding to the two receivers.

Similar to the formulation of the coupling coefficient in the single-receiver model, by referring to the magnetic reluctance model as shown in Fig. 6, the coupling coefficient k_1 for the two-receiver mechanism can be expressed as follows:

$$k_1 = \frac{1}{1 + \frac{R_{IH+2R_g}}{R_{IL}}}. \tag{12}$$

Through comparison of the magnetic model of the two-receiver mechanism, it becomes apparent that the coupling coefficient for the second receiver k_2 is equivalent to k_1

$$k_1 = k_2. \tag{13}$$

Compared with (10), it is apparent that, under the assumption of where the air reluctance on the primary side is neglected, the coupling coefficients of both mechanisms are identical. Consequently, the coupling coefficients for both mechanisms are the same, and this can be expressed by

$$k = k_1 = k_2. \tag{14}$$

C. No-Receiver Mechanism

In the no-receiver mechanism, the basic cell becomes an inductor as shown in Fig. 7. The coupling coefficient is 0 because no secondary side magnetic core is coupled to the primary side. This mechanism is a stand-by operation or no load, as the whole system is in a state of readiness, waiting for the receivers to transfer power. Furthermore, the magnetic flux density in this mechanism is considerably weaker than that of single- and two-receiver mechanisms as illustrated in Fig. 6, as the equivalent reluctance of the magnetic circuit is much higher. This is because all the magnetic flux passes through the low-permeability *I core.*

Since the R_{air} of the primary side has been neglected, only one path inside the magnetic core is formed. The equivalent permeability of a magnetic core is

$$u_{\text{eq}} = \frac{u_L u_H (2L + 2H + W_b)}{2Lu_H + 2Hu_L + W_b u_L}. \tag{15}$$

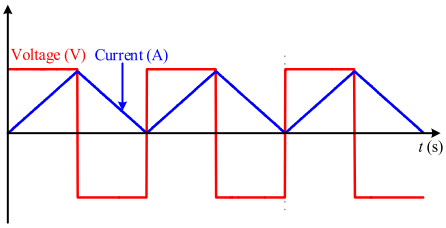

Fig. 8. Input voltage and current of the on-receiver mechanism in an ideal state.

The magnetomotive force is

$$mmf = 0.4\pi N I_m \tag{16}$$

where N is the number of turns and I_m is the magnetizing current.

Flux density is then yielded

$$B = \frac{0.4\pi N I_m u_{eq}}{2L + 2H + W_b} \tag{17}$$

which is very important for selecting a magnetic core.

The ac voltage source supplies the inductor, and no power is transferred. For the ideal state, the input voltage and current waveforms are shown in Fig. 8.

Although no power is transferred, there is still power loss on the conduction lines caused by the magnetizing current. The salient point of the configuration is the usage of high magnetic permeability to confine the flux which reduces the leakage flux in the surrounding and focus the flux to couple to the load. Power losses in the stand-by mechanism are analyzed in the following section.

D. Output Voltage of the Receivers

Using Faraday's Law, the input voltage V_{Lp} of the transmitter's coil can be represented

$$V_{Lp} = \frac{d\left(\emptyset_1 + \emptyset_2 + \emptyset_3\right)}{\mathrm{dt}}. \tag{18}$$

By referring to (6), the output voltage of each receiver can be related to the turns ratio and the coupling coefficient as follows:

$$V_{o1} = n_1\, k_1 V_{Lp} \tag{19}$$

$$V_{o2} = n_2\, k_2 V_{Lp} \tag{20}$$

where n_1 and n_2 are the turns ratios of the secondary to the primary side. Similarly, the output voltage in the one-receiver mechanism can be calculated using the same equation.

IV. Generalization of the Proposed WPT Cells

A. Generalized Scheme

The basic cells can be generalized by tapping more receivers in the secondary as depicted in Fig. 9(b). Subsequently, the generalized cells can be connected in paralleled to form a magnetic wall/panel, as shown in Fig. 9(c). Since all the basic cells are in the same state, i.e., with the same topology of magnetic cores and the ac source, the voltages at each receiver will be identical if a single turn number is adopted in the primary transmitter and secondary receiver. The ac power can be obtained by using

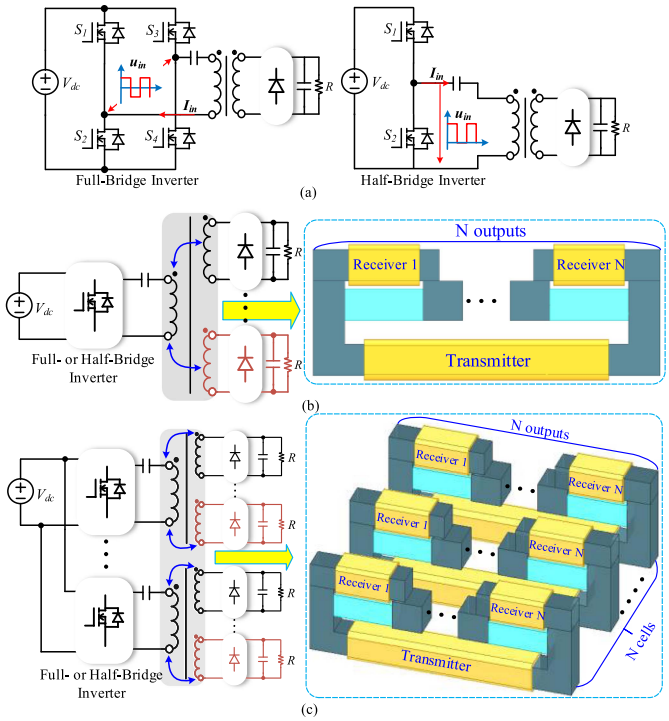

Fig. 9. Multiple outputs expansion schematic. (a) Inverter topologies. (b) Generalization of basic cells. (c) Multiple outputs magnetic panel construction.

half- or full-bridge inverter, as shown in Fig. 9(a). Additionally, Different output voltages can be achieved by varying the number of windings on the secondary side.

B. Driver for the Magnetic Wall

The proposed near-field WPT system can be driven by either half- or full-bridge inverter. The voltage rating of the transistors of the H-bridge is of course equal to V_{dc}. The voltage ratings of the output diodes of each receiver are equal to its output. The current rating is determined by the output loading derived from the load resistance. For a system with multiple cells, more inverters can be connected in parallel to the input source. The driving signals for the inverter are provided by microcontroller TMS320F28335. The switching frequency of the experiment is selected to be the mid-point of the usual WPT frequency range of the charging system. 80 kHz is presently used. The circuitry of half- or full-bridge inverters is illustrated in Fig. 9(a).

V. Design Considerations and Loss Analysis

A. Magnetic Core Selection

As previously discussed, the proposed WPT system contains magnetic cores with two different permeabilities, and the selection of μ_H and μ_L should be made according to specific guidelines.

1) μ_H must be sufficiently high to accommodate a larger amount of magnetic flux. In order to improve the coupling and ensure a low reluctance magnetic path for the flux conduction when a receiver is placed to the magnetic

distribution circuit, it is recommended to position the receivers in high permeability regions.

2) The lower permeability *I core* is selected according to the promise between the low leakage during the loading condition and the unloaded condition. The selection of μ_L should be around 5% to 10% of μ_H that in turn define R_{uL}, as depicted in Fig. 4, with consideration given to the coupling coefficient.
3) To ensure good coupling to the load, the saturation flux density of the magnetic materials must exceed the value specified in (17).

In this simulation, the magnetic cores are selected with initial permeability 3300 (μ_H) and 40 (μ_l), based on the criteria described above. The whole geometry is consistent with that described in Section III-A. Furthermore, since the proposed core-based WPT system operates at a high frequency, particular consideration is needed for the windings of the transmitter and receiver coils to reduce losses and further improve the performance of the magnetic power distribution system. Therefore, the high-frequency winding techniques can be a reference to the work [25].

B. Loss Analysis

Power loss is a typical issue for many WPT systems. The present analysis is based on high permeability magnetic cores so as to reduce the leakage and also the magnetic loss is assumed to be low to make the analysis simple. Furthermore, the copper conduction loss is designed to be low because the magnetizing current is lower because the high permeability magnetic cores are used, which is an advantage. This is in contrast to the coreless WPT system, which has higher conduction losses due to the high magnetizing current injected into the primary coils.

For the two-receiver mechanism, the efficiency analysis is shown below. The output power is basically a summation of each output and is related to the RMS value of the output current I_{o1} and I_{o2} with resistive load R_{O1} and R_{O2}, and the output power is given by

$$P_0 = I_{o1}^2 \ R_{O1} + I_{o2}^2 \ R_{O2}. \tag{21}$$

The conduction power loss is simply described by the *I* square *R*. With input current I_{in}, I_{o1} and I_{o2}, And the magnetizing current I_{m}, and the equivalent resistance of the primary and the two secondary coils, denoted by r_0, r_1 and r_2, respectively,

$$\begin{aligned} P_{\mathrm{loss}} &= P_{r0} + P_{r1} + P_{r2} \\ &= I_{\mathrm{in}}^2 \ r_0 + I_{o1}^2 \ r_1 + I_{o2}^2 \ r_2 \\ &= (\ I_{o1} \cdot n_1 k_1 + I_{o2} \cdot n_2 k_2 + I_m)^2 \ r_0 + I_{o1}^2 r_1 + I_{o2}^2 r_2. \end{aligned} \tag{22}$$

Theoretical efficiency

$$\eta = \frac{P_o}{P_o + P_{\mathrm{loss}}} = \frac{1}{1 + \frac{P_{\mathrm{loss}}}{P_o}}. \tag{23}$$

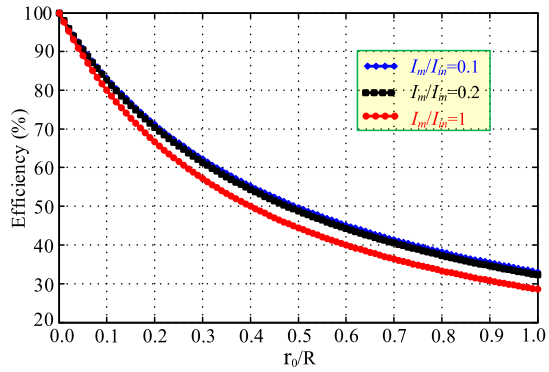

Fig. 10. Theoretical efficiency vs $\frac{r_0}{R}$ ($n = 1$ and $k = 1$) with various ratios between I_m and I_{in}.

Assume that $n_1 = n_2 = n$, $R_{O1} = R_{O2} = R$, then dc resistance r_1 equals r_2, I_{o1} equals I_{o2}

$$r_1 = r_2 = \frac{r_0}{n} \tag{24}$$

$$I_{o1} = I_{o2} = \frac{I_{\mathrm{in}}}{kn}. \tag{25}$$

Equations (21) and (22) can be simplified and the transfer efficiency can be derived

$$\eta = \frac{1}{1 + \left(2\mathrm{n}^2\mathrm{k}^2 + 2\mathrm{n}^2\mathrm{k}^2 \frac{I_m}{I_{in}} + \frac{1}{2} + \frac{1}{\mathrm{n}}\right) \frac{r_0}{\mathrm{R}}}. \tag{26}$$

For some given parameters, theoretical efficiency is plotted in Fig. 10.

C. Loss at No-Receiver Mechanism and the Number of Turns

The power loss under the no-receiver mechanism is expressed as follows:

$$P_l = I_m^2 \ r_0 = I_m^2 \ \frac{\rho N_p 4 w_a}{S_0} \tag{27}$$

where ρ denotes the resistivity of the windings, S_0 represents the cross-sectional area of the winding, and N_p denotes the number of primary turns, which can be expressed as

$$N_p = \frac{R_{\mathrm{eq}} B A_e}{0.4\pi I_m}. \tag{28}$$

By substituting (28) into (27), power loss under the no-receiver mechanism can be obtained

$$P_l = \frac{\rho}{N_p} \frac{4 w_a}{S_0} \frac{(R_{\mathrm{eq}} B A_e)^2}{(0.4\pi)^2}. \tag{29}$$

This, the number of primary turns, N_p, is determined by the allowed no-load loss and the magnetic core and winding parameters

D. Losses of Converter Analysis

The losses generated by the inverter including the conduction losses and the switching losses of the MOSFETs, also has an impact on the system efficiency. It is assumed that the system is driven by the H-bridge inverter.

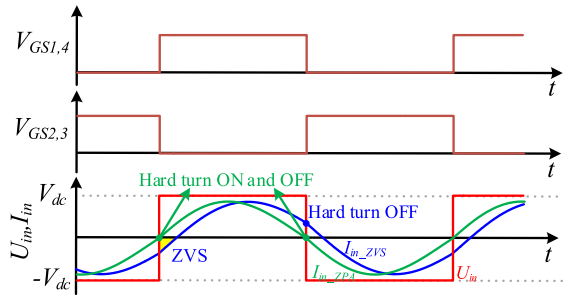

Fig. 11. Soft switching realization waveforms.

1) *Conduction Losses of MOSFET:* When the H-bridge inverter is operating, both switches will be turned ON at the same time. The conduction losses of the MOSFET can therefore be calculated by

$$P_{\text{con}} = 2\, I_{\text{in}}^2\ r_S \tag{30}$$

where r_S is the equivalent on-resistance of one MOSFET in the H-bridge inverter.

2) *Switching Losses of MOSFET:* When the system operates at zero phase angle (ZPA) condition, the switches behave as hard-ON and hard-OFF, as shown in Fig. 11, where two switches are turned ON and two switches are turned *OFF* at each output cycle. As described in [26] and [27], the switching losses are related to energy loss E_{sw} during the MOSFET's transition, as well as switching frequency f. It is given by

$$E_{\text{sw}} = \int_0^{t_{\text{sw}}} v_{ds}\,(t)\, i_d\,(t)\, dt \tag{31}$$

$$P_{\text{sw}} = V_{ds\_\text{avg}}\ I_d 4 \left(\frac{E_{on} + E_{off}}{V_D I_D}\right) f \tag{32}$$

where E_{on} and E_{off} are turn-ON and turn-OFF energy of MOSFET. V_{ds_avg} is the average voltage stress of the MOSFET during one switching cycle. V_D and I_D are drain-source voltage and current, respectively, which are provided by the manufacturer.

However, by reasonably setting the value of the compensation capacitor so that the input current slightly lags the input voltage, as shown in Fig. 11, zero-voltage switching (ZVS) of the MOSFETs can be achieved to optimize the switching losses. Furthermore, the VA rating for the MOSFETs can be maintained at a reasonable value [28]. Hard turn-OFF loss still occurs in MOSFETs, and the reverse recovery losses of the anti-parallel diode should also be considered. The switching losses can therefore be optimized as

$$P_{\text{sw}} = 2\sqrt{2} V_{\text{dc}} I_{\text{in}} \left(\frac{\text{E}_{\text{off}}}{V_D I_D} + \frac{Q_{DD}}{I_{RD}}\right) f \tag{33}$$

where Q_{DD} and I_{RD} are the reverse recovery charge and the reference current of anti-parallel diode, respectively, which are provided by the manufacturer.

3) *Power Loss of Passive Rectifier*: the power loss of the passive rectifier is mainly from the conduction loss of diodes [26], [27]. It can be calculated by

$$\begin{aligned} P_{rec} &= \frac{4}{T} \int_0^{\pi} \left(V_F + r_D i_{\text{rec}\_i}\right) i_{\text{rec}\_i} d\,(\omega t) \\ &= \frac{4\sqrt{2}}{\pi}\, V_F I_{\text{rec}\_i} + 2 r_D I_{\text{rec}\_i}^2 \end{aligned} \tag{34}$$

where V_F is the forward voltage of the diode; r_D is the equivalent on-resistance of the diode; and i_{rec_i} is the input current of the ith rectifier.

E. Core Losses Analysis

The core loss per unit volume of a magnetic core can be estimated by the Steinmetz empirical equation [29]. It is given by

$$P_V = K_h\ f^{\alpha} B^{\beta} \tag{35}$$

where K_h, α, and β are the Steinmetz parameters. f is the frequency of the sinusoidal source. B is the magnitude of the time-varying sinusoidal flux density in the magnetic core. When the magnetic core is selected, the Steinmetz parameters are fixed values.

From (35), it indicates that the core loss per unit volume of a magnetic core is determined by the frequency f and the peak magnetic flux density B. Generally, the frequency f is constant for a system. Therefore, the total core loss can be calculated by integrating the volume of the system's magnetic cores, as follows:

$$\begin{aligned} P_{\text{core}} = K_h\ f^{\alpha} &\left(\int_{V_{TX}} B_{TX}^{\beta} dV + n \int_{V_{RX}} B_{RX}^{\beta} dV\right) \\ &+ m {K'}_h f^{\alpha'} \int_{V_{L\_I\text{core}}} B_{L\_I\text{core}}^{\beta'} dV \end{aligned} \tag{36}$$

where n denotes that there are n receivers on the receiver side. m means that there are m low-permeability I *cores* that are not bypassed.

The magnetic flux density in the magnetic core is proportional to the ampere-turns of the coil and inversely proportional to the magnetic flux length, i.e.,

$$B \propto \frac{NI}{l} \tag{37}$$

where l is the effective magnetic flux length of magnetic cores.

From (37), it shows that when the system is established, the total core loss is positively related to the current of the coil.

VI. Comparison With Traditional Structure

In this section, a comparison is made between the proposed structure and the air-based structure in the implementation of the multiple output structure to highlight the advantages of the proposed coupling structure and to further explain the contribution of this article. The air-based structures include coreless single-output WPT system [30], core-based single-input IPT system [31], multiple-input multiple-output IPT system [32], and single-input multiple-output WPT system [33]. The comparison parameters are given in Table I, where 'Flexibility' means

TABLE I
COMPARISON WITH AIR-BASED COUPLING STRUCTURE

Coupling type	Air				Magnetic core
Article	Zhong and Hui [30]	Gaona et al. [31]	Vu et al.[32]	Sun et al. [33]	This article
Number of input voltage	N	N	1	1	1
Number of the primary coil	N	N	N	1	1
Leakage	High	High	High	High	Low
Coupling coefficient	0.0689	0.297	0.20-0.24	0.20	0.1-0.6
Weight	Light	Middle	Middle	Light	Heavy
Flexibility	INF.	INF.	INF.	F.	F.
Dimension of the primary coil	Small	Small	Small	Large	Small

"F"and "INF." mean flexibility and inflexibility, respectively.

the freedom to increase or decrease the number of receivers and to freely place receivers in different positions.

As given in Table I, when extended to a multiple output structure, the works in [30], [31] require N voltage sources, while the work in [32] requires only one input voltage source by using the parallel drive power supply. However, due to the one-to-one coupling manner, they all need N transmitters, which significantly increases the cost of the system. The proposed structure and the structure in [33] use a one-to-many coupling method, requiring only a single voltage source and transmitter. But, the magnetic flux is conducted through air in air-based systems, so there is severe magnetic leakage, typically resulting in a low coupling coefficient. The coupling coefficient can relatively improve by adding magnetic cores to the transmitter and receiver coils [31], [32], which is still inferior to the proposed coupling structure. As depicted in Fig. 4, the coupling coefficient of the proposed system can be reasonably chosen between 0.1 and 0.6 by simply controlling the low permeability of *I cores* integrated into the transmitter, resulting in a good and wide range of coupling coefficient, and the magnetic leakage is very low due to the effect of the magnetic core confining the magnetic flux. Even if there are no receivers on the secondary side, the magnetic flux will all be confined in the magnetic cores and will not be released into the air, as analyzed in Fig. 7. Thus, low magnetic leakage and strong coupling coefficient make it easier and more flexible for the proposed system to power in-house electrical devices over a large area. However, the use of magnetic cores does lead to the problem that the weight and volume of the proposed structure will be larger than the air-based WPT system. Thus, the proposed structure is not suitable for portable devices such as consumer electronics. It is more suitable for powering large devices such as lights, fans, audio sets and monitors, etc. in large areas such as residences or offices.

On the other hand, a flexible and convenient method to output energy is highly preferable for the users. In the air-based WPT system described in [33], the receivers can be freely coupled to the transmitter, allowing them to output power. However, the dimension of these receiver coils is limited to that of the transmitter coil. When many devices in a large area need to be powered, the transmitter coil must be very large, making this method impractical.

Alternatively, works in [30], [31], and [32] use small transmitter coils, but require multiple transmitters. Additionally, the receivers must be coupled to their specific transmitter at its resonant frequency, which limits their flexibility. In contrast, the proposed structure allows for the easy extension of multiple outputs by simply extending the arms of the *C core* in the transmitter. This enables multiple outputs to easily provide energy over a large area while maintaining an unchanged transmitter coil.

Therefore, the proposed structure can just use a single transmitter coil and employ different permeability magnetic cores to guide the magnetic flux, so that the energy output points (i.e., P_1&P_2 or P_2&P_3 in Fig. 2) can be set in a specific area (i.e., the location of the in-house electrical devices). Thus, the size of the transmitter coil can be optimized, and the leakage flux in the air can be greatly reduced or even eliminated. Therefore, compared to traditional air-based WPT system or wired plug-in power distribution, the receiver with a high-permeability core of the proposed system can be freely tapped on the energy output points such as P_1&P_2 or P_2&P_3 and bypass the low-permeability *I core* of the transmitter, and then coupled to the transmitter, which greatly increases the flexibility of harvesting power.

VII. HARDWARE DESCRIPTION AND PERFORMANCE

A. Test of One Basic Cell With Three Output

By referring to Fig. 9(b), a downscale basic cell with three receivers is built as shown in Fig. 12. Two kinds of high-frequency Zn-Mn ferrite magnetic cores are used. One is P95 with an initial permeability of 3300 (μ_H), a saturation flux density 0.53 mT and a Curie temperature greater than 215 °C. And the other is R40 with an initial permeability of 40 (μ_L), a saturation flux density 0.25 mT and a Curie temperature greater than 300 °C. The pole's cross-sectional area and height are consistent with the simulation values presented in Section III-A. The length air gap l_g is approximately 2.5 mm. The wingdings are arranged in a ratio of n_1:n_2:n_3 = 1:1:1. The high-frequency eddy current loss in the winding is reduced by constructing all the winding using the 1.2 mm^2 Litz wire. The parasitic resistance of the coil for the transmitter and receivers are 0.07 Ω, 0.065 Ω, 0.062 Ω, and 0.063, respectively. The input dc voltage for the full-bridge inverter is 40 V for small output power and 100 V for high output power experiment. For a wide range of output power tests, the input voltage varies from 40 to 100 V. An 80 kHz driving signal with a duty cycle of 0.5 is employed to drive the SIC inverter (F4-23MR12W1M1_B11). Three 100 Ω resistors with a power rating of 100 W each are connected in the outputs in the small output power.

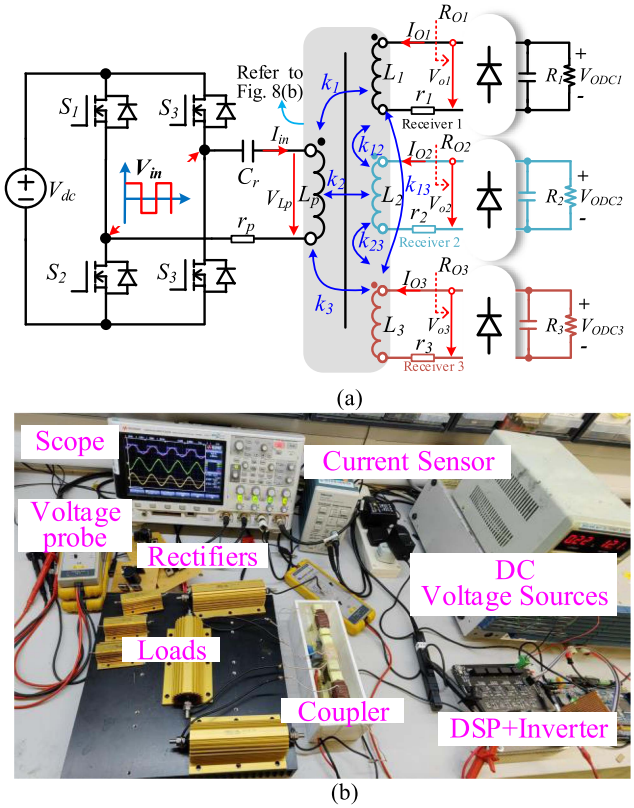

Fig. 12. Magnetic distribution setup with three receivers. (a) Diagram of the proposed near-field WPT circuit. (b) Experimental bench for the proposed prototype.

Fig. 13 shows the output waveforms of three receivers of the prototype with three pure resistive loads 100 Ω. When the three receivers are connected in isolation, the output waveforms are shown in Fig. 12(a). The RMS value of the V_{O1}, V_{O2}, and V_{O3} are 65.5, 62.4, and 69.9 V, respectively. To boost the output voltage, the three outputs can be connected in series, which will produce a voltage of higher amplitude. As shown in Fig. 13(b), the RMS value of the output voltage is 197 V when three receivers are connected in series. It can be seen that the output voltage in series is approximately equal to the sum of the output voltage separately. Moreover, with the resonant capacitor, the input voltage and current are in phase, which indicates that the system achieved the zero-phase-angle characteristics. Therefore, the system is capable of transferring the power to receivers with maximum transfer efficiency. Furthermore, the RMS value of the input voltage of the transmitter coil V_{Lp} is 373 V. Based on the analysis of (19) and (20), the coupling coefficients are 0.18, 0.17, and 0.19 for the three receivers, respectively. It is consistent with the analysis of Fig. 4 in Section II-A. Fig. 13(c) shows the result of standby mode. The RMS value of the input current and the input voltage of the transmitter's coil is 2.99 A and 232 V, respectively. In addition, the phase difference between them is 89.21°. It can therefore be calculated that the loss of the standby mode is 9.56 W.

In order to evaluate the dc output performance of the system, a bridge rectifier was added to each receiver. The experimental results are shown in Fig. 14. When each of the three receivers

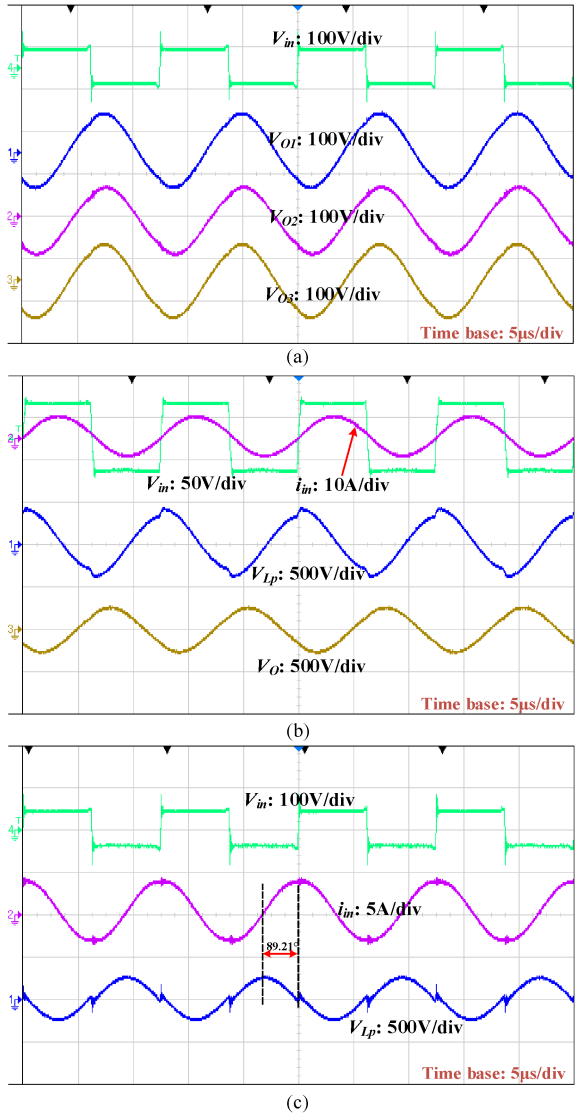

Fig. 13. Experimental results without rectifiers. (a) Output voltage of three receivers. (b) Output voltage of three receivers in series. (c) Stand-by mode.

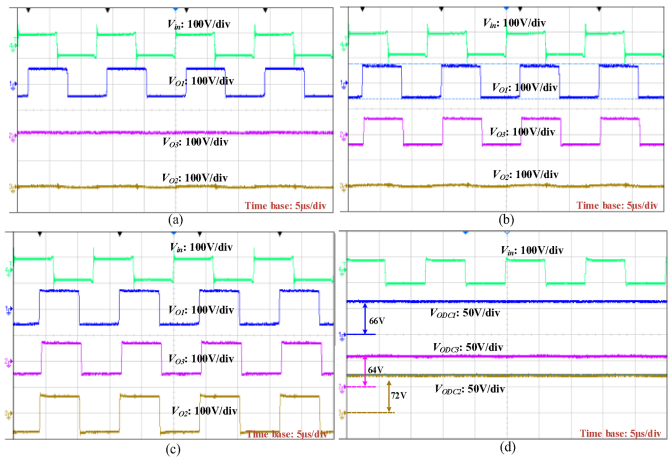

Fig. 14. Experimental results with rectifiers. (a) One-receiver mode. (b) Two-receiver mode. (c) Three-receiver mode. (d) DC output voltage.

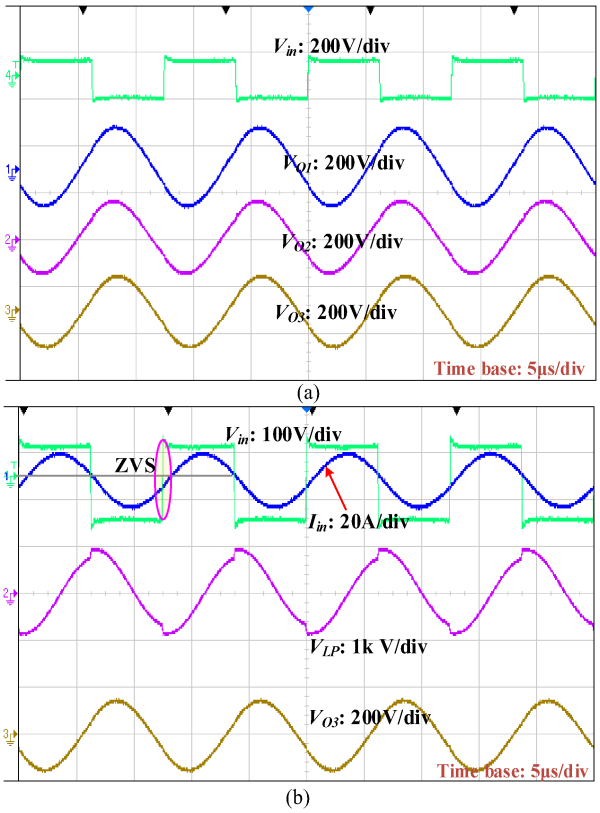

Fig. 15. Experimental results without rectifiers. (a) Output voltage of three receivers. (b) Input voltage and current and the voltage of L_p and receiver3.

is added in turn, the peak-to-peak values of the input voltage of the rectifier are 122 V for the single receiver in Fig. 14(a), 140 and 135 V for the two receivers in Fig. 14(b), and 162, 158, and 167 V for the three receivers in Fig. 14(c), respectively. From the results above, as the number of receivers increases in sequence, the output voltage of each receiver increases as well. Because the magnetic core used in each receiver has a high enough permeability characteristic to bypass the low-permeability magnetic core on the primary side, thereby increasing the coupling coefficient of the system, which in turn increases the output voltage of each receiver. The dc output voltages of the three receivers are 66, 64, and 72 V, as shown in Fig. 14(d).

B. High Output Power Performance Verification

In order to verify the performance of the system at high output power, the three receivers are respectively connected to pure resistors with a resistance of 68 Ω and a power rating of 300 W. when the input voltage is fixed to 100 V, the output waveforms of the system are shown in Fig. 15. Fig. 15(a) shows the results of the input voltage and output voltage of three receivers. The RMS values of receivers are 107, 117, and 106 V, respectively. The voltage of the primary coil V_{Lp} is shown in Fig. 15(b), and its RMS value is 595 V. Thus, the coupling coefficient can be calculated as 0.18, 0.196, and 0.178, respectively, which verified that the measured coupling coefficients are still consistent with the theoretical ones of Fig. 4 in large output power when the air gap is 2.5 mm. In addition, by reasonably setting the value of

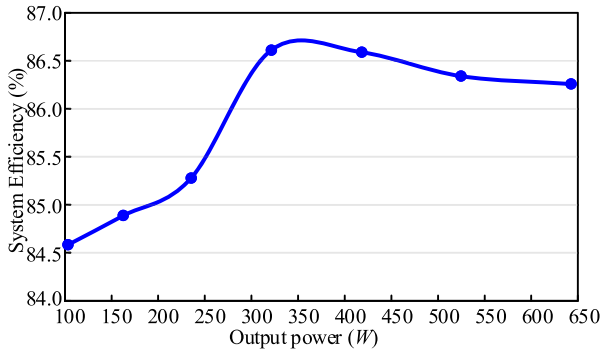

Fig. 16. System efficiency versus the output power.

the resonant capacitor and making the phase of the input current lag behind the phase of the input voltage, ZVS can be achieved and the VA rating of the switches can be effectively reduced, as shown in Fig. 15(b).

The system efficiency was measured and its efficiency versus the output power from 100 to 643 W is shown in Fig. 16. The maximum efficiency occurs at the system output power of 321 W. When the output power of the system continues to increase, the system efficiency decreased slightly. This is because the current of the system increased with the increase of the output power, which results in increases in core loss and other losses. The measured power loss distribution is shown in Fig. 17. According to the experimental power loss distribution, the power losses proportion of the coupler increased obviously, which is mainly generated by the core loss. Specifically, when the output of the system is 642.6 W, the measured and calculated power loss distributions are shown in Fig. 17(b) and (c), where the measured results are obtained by making the difference between the measured input and output power of each unit of the system, while the calculation results are obtained directly by substituting the input and output currents and voltages of the experiment into the equations analyzed in Section V. Taking the power losses of the coupler as an example, $\Delta P_{\text{coupler}}$ is first measured, then the coil loss P_{coil} is obtained based on the input and output currents and (22), and finally the core loss P_{core} can be obtained by $P_{\text{core}} = \Delta P_{\text{coupler}} - P_{\text{coil}}$. For the calculated core loss, the magnetic field density B is calculated with the help of ANASYS Maxwell, and then substituted into (36) to calculate the core power loss. For the inverter and rectifiers, the measured and calculated power loss results are also obtained following this method.

C. Misalignment

When there is a misalignment between the receivers and transmitter, including lateral and vertical misalignment, the output voltages and efficiency of the system at a fixed input voltage of 100 V are shown in Fig. 18, where the horizontal coordinate in Fig. 18(a) is defined as the ration of the misalignment distance L_x to the width of receiver W_a defined in Section II, and the horizontal coordinate in Fig. 18(b) is defined as the number of air gap l_g defined in Section III. It indicates that with the increase of the misalignment distance, the output voltages and the system

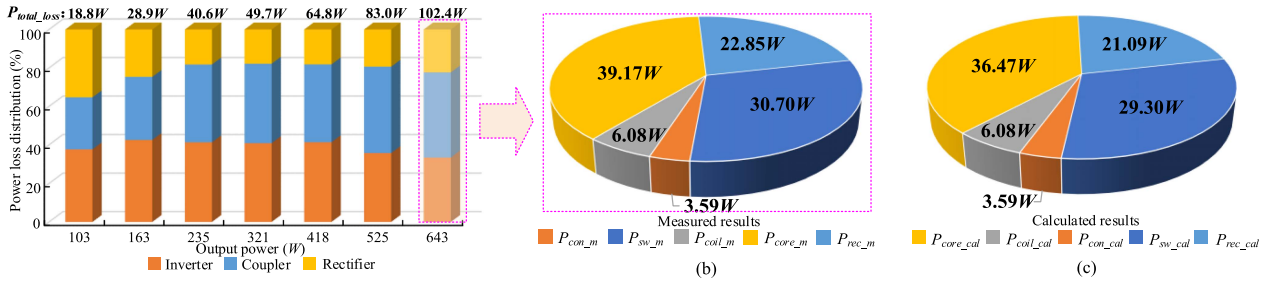

Fig. 17. Power loss distribution. (a) Power loss distribution versus the output power. (b) Measured power losses at the output power of 643 W. (c) Calculated power losses at the output power of 643 W.

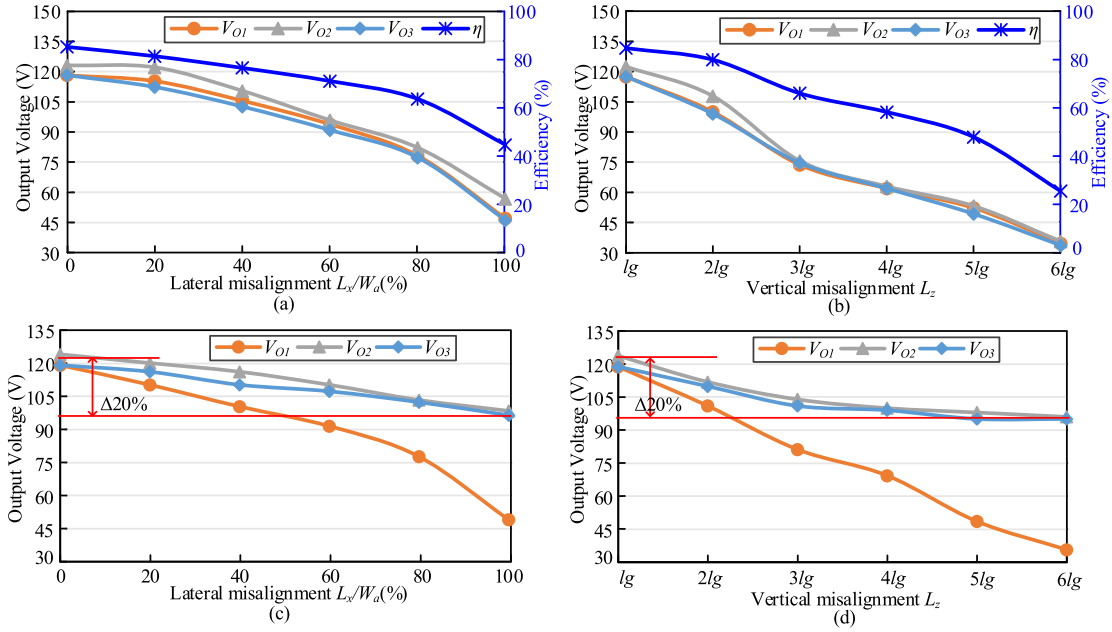

Fig. 18. Output voltage of receivers versus misalignment distance. (a) Lateral misalignment. (b) Vertical misalignment. (c) Lateral misalignment of receiver 1. (d) Vertical misalignment of receiver 1.

efficiency decrease, which is caused by the increase of the air reluctance between the transmitter and receivers. According to the equations of (5) and (10), the increase in air reluctance leads to a lower coupling coefficient of the system thus reducing the output voltages. Due to the effect of the core's directing flux, when lateral misalignment happens, i.e., air gap length l_g is constant, the output voltage of the receiver can be maintained relatively stable at 20% of the misalignment distance, as shown in Fig. 18(a). When the misalignment distance increase continuously, the output voltage decreases noticeably. By appropriately increasing the cross-sectional area of the transmitter's core, the tolerance towards lateral misalignment can be improved effectively. As depicted in Fig. 18(a) and (b), the proposed system is sensitive to vertical misalignment. This is because when the vertical misalignment increases, the low-permeability *I core* conducts more flux, which weakens the coupling between the transmitter and receivers. However, when the receiver is integrated in the electrical devices, the air gap distance l_g between the transmitter and the receiver will be fixed to the package thickness at this time.

In addition, when the misalignment happens in one of the receivers in the system and the others remain stable, the output voltages of receivers are shown in Fig. 18(c) and (d). When misalignment happens in receiver1 either in the lateral or vertical direction, the output voltages of receivers without misalignment are reduced by 20%. This is because when receiver1 is misaligned over a large distance, more magnetic flux can be conducted by its parallel low-permeability *I core*, ensuring a good coupling coefficient between the other receivers and transmitter. It also benefited from the use of the low-permeability *I cores*, which is impossible for air core from the analysis in Fig. 5(b). Again, the misalignment tolerance in the lateral direction is better than that in the vertical direction, where the voltage drop is less than 8.8% within 50% of the misalignment distance in the lateral direction.

D. Test of Extension of the Magnetic System

To test the magnetic panel, a total of seven basic cells are connected in parallel, and 10 LED lights are utilized as the load, as

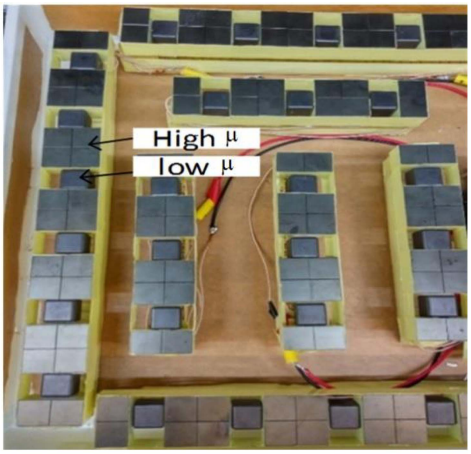

(a)

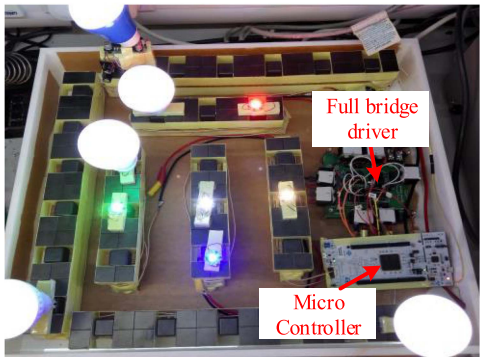

(b)

Fig. 19. Magnetic wall system. (a) Seven basic cells. (b) System supplies multiple loads.

shown in Fig. 19. In order to increase the surface area for power harvesting, two *cube cores* are integrated, effectively doubling the cross-sectional area. Moreover, the length of the μ_L core is shortened, thereby reducing the total reluctance. The results demonstrate that power can be efficiently delivered wirelessly, and the ten LED lights operate steadily, drawing a total power of 10 W.

VIII. Conclusion

Magnetic power distribution using a near field is proposed. It is not based on the air core or air core with the assistance of ferrites to provide the wire power transfer, instead, it is using a magnetic conductor to conduct the power through magnetic flux distribution. The salient point is that the power transfer is all through conductive magnetics. The performance characteristics including efficiency and coupling coefficient with the physical sizes have been formulated. A maximum system efficiency 86.6% is achieved at output power 321 W of the basic unit with three receivers. And high system efficiency can be maintained over a wide range of output power. The misalignment characteristics were fully tested and the results showed that the tolerance of lateral misalignment was better than that of vertical misalignment. Moreover, when there is a certain receiver is misaligned in the system, a small influence on the output voltages of other receivers without misalignment is observed. Furthermore, the unit has been conducted with multiple tests and has been installed in the laboratory for the investigation of magnetic power distribution. The results presented verified the operation and confirmed it is a possible power transfer as an alternative to the electrical power transfer.

References

[1] Z. Zhang, H. Pang, A. Georgiadis, and C. Cecati, "Wireless power transfer—An overview," *IEEE Trans. Ind. Electron.*, vol. 66, no. 2, pp. 1044–1058, Feb. 2019.

[2] W. Huang, Y. Zhang, F. Gao, and Y. Tang, "Double-sandwich magnetic coupling structure design for dual-LCL wireless charging system in EV applications," *IEEE Trans. Veh. Technol.*, vol. 72, no. 3, pp. 3239–3249, Mar. 2023.

[3] L. Zhu, L. Wang, X. Wu, C. Zhao, and L. Yu, "Precise modeling and design of self-resonant helical coils for high-efficiency mid-range wireless power transfer system," *IEEE Trans. Power Electron.*, vol. 38, no. 6, pp. 7848–7862, Jun. 2023.

[4] Y. Li, R. Mai, L. Lu, T. Lin, Y. Liu, and Z. He, "Analysis and transmitter currents decomposition based control for multiple overlapped transmitters based WPT systems considering cross couplings," *IEEE Trans. Power Electron.*, vol. 33, no. 2, pp. 1829–1842, Feb. 2018.

[5] D. Ahn and S. Hong, "Effect of coupling between multiple transmitters or multiple receivers on wireless power transfer," *IEEE Trans. Ind. Electron.*, vol. 60, no. 7, pp. 2602–2613, Jul. 2013.

[6] J. Shin et al., "Design and implementation of shaped magnetic-resonance-based wireless power transfer system for roadway-powered moving electric vehicles," *IEEE Trans. Ind. Electron.*, vol. 61, no. 3, pp. 1179–1192, Mar. 2014.

[7] D.-H. Kim and D. Ahn, "Maximum efficiency point tracking for multiple-transmitter wireless power transfer," *IEEE Trans. Power Electron.*, vol. 35, no. 11, pp. 11391–11400, Nov. 2020.

[8] F. Zhao, J. Jiang, S. Cui, X. Zhou, C. Zhu, and C. C. Chan, "Research on bipolar non-salient pole transmitter for high-power EV dynamic wireless power transfer system," *IEEE Trans. Power Electron.*, vol. 37, no. 2, pp. 2404–2412, Feb. 2022.

[9] J. Feng, Q. Li, F. C. Lee, and M. Fu, "LCCL-LC resonant converter and its soft switching realization for omnidirectional wireless power transfer systems," *IEEE Trans. Power Electron.*, vol. 36, no. 4, pp. 3828–3839, Apr. 2021.

[10] L. Zhou et al., "Efficiency optimization of LCC-S compensated multiple-receiver bidirectional WPT system for stackers in automated storage and retrieval systems," *IEEE Trans. Power Electron.*, vol. 37, no. 12, pp. 15693–15705, Dec. 2022.

[11] C. Jiang, K. T. Chau, W. Liu, C. Liu, W. Han, and W. H. Lam, "An LCC-compensated multiple-frequency wireless motor system," *IEEE Trans. Ind. Inform.*, vol. 15, no. 11, pp. 6023–6034, Nov. 2019.

[12] J. Huh, S. W. Lee, W. Y. Lee, G. H. Cho, and C. T. Rim, "Narrow-width inductive power transfer system for online electrical vehicles," *IEEE Trans. Power Electron.*, vol. 26, no. 12, pp. 3666–3679, Dec. 2011.

[13] V. T. Kilic, E. Unal, E. Gonendik, N. Yilmaz, and H. V. Demir, "Strongly coupled outer squircle–inner circular coil architecture for enhanced induction over large areas," *IEEE Trans. Ind. Electron.*, vol. 63, no. 12, pp. 7478–7487, Dec. 2016.

[14] S. Y. Choi, J. Huh, W. Y. Lee, and C. T. Rim, "Asymmetric coil sets for wireless stationary EV chargers with large lateral tolerance by dominant field analysis," *IEEE Trans. Power Electron.*, vol. 29, no. 12, pp. 6406–6420, Dec. 2014.

[15] W. Roshen, "Ferrite core loss for power magnetic components design," *IEEE Trans. Magn.*, vol. 27, no. 6, pp. 4407–4415, Nov. 1991.

[16] S. C. B. Gony, J. Hill, and F. Pottier, "A new generation of nanocrystalline magnetic cores with very low magnetic losses," in *Proc. Int. Exhib. Conf. Power Electron., Intell. Motion, Renew. Energy Energy Manage.*, 2016, pp. 1–7.

[17] N. Alatawneh, T. Rahman, D. A. Lowther, and R. Chromik, "Design and analysis of a toroidal tester for the measurement of core losses under axial compressive stress," *J. Magn. Magn. Mater.*, vol. 432, pp. 519–526, 2017.

[18] J. G. Zhu, S. Y. R. Hui, and V. S. Ramsden, "A generalized dynamic circuit model of magnetic cores for low- and high-frequency applications. I. Theoretical calculation of the equivalent core loss resistance," *IEEE Trans. Power Electron.*, vol. 11, no. 2, pp. 246–250, Mar. 1996.

[19] F. D. Tan, J. L. Vollin, and S. M. Cuk, "A practical approach for magnetic core-loss characterization," *IEEE Trans. Power Electron.*, vol. 10, no. 2, pp. 124–130, Mar. 1995.
[20] Y. Guo, Y. Zhang, S. Li, C. Tao, and L. Wang, "Load parameter joint identification of wireless power transfer system based on the DC input current and phase-shift angle," *IEEE Trans. Power Electron.*, vol. 35, no. 10, pp. 10542–10553, Oct. 2020.
[21] M. Wu et al., "A dual-sided control strategy based on mode switching for efficiency optimization in wireless power transfer system," *IEEE Trans. Power Electron.*, vol. 36, no. 8, pp. 8835–8848, Aug. 2021.
[22] K. Li, S.-C. Tan, and R. S. Y. Hui, "On beat frequency oscillation of two-stage wireless power receivers," *IEEE Trans. Power Electron.*, vol. 35, no. 12, pp. 12741–12751, Dec. 2020.
[23] Z. Zhou, L. Zhang, Z. Liu, Q. Chen, R. Long, and H. Su, "Model predictive control for the receiving-side DC–DC converter of dynamic wireless power transfer," *IEEE Trans. Power Electron.*, vol. 35, no. 9, pp. 8985–8997, Sep. 2020.
[24] Z. Dong, S. Liu, X. Li, Z. Xu, and L. Yang, "A novel long-distance wireless power transfer system with constant current output based on domino-resonator," *IEEE J. Emerg. Sel. Topics Power Electron.*, vol. 9, no. 2, pp. 2343–2355, Apr. 2021.
[25] K. W. E. Cheng and P. D. Evans, "Calculation of winding losses in high frequency toroidal inductors using multi-strand conductors," *IEE Proc.-Elect. Power Appl.*, vol. 142, no. 5, pp. 313–322, Sep. 1995.
[26] N. X. Bac, D. M. Vilathgamuwa, and U. K. Madawala, "A SiC-based matrix converter topology for inductive power transfer system," *IEEE Trans. Power Electron.*, vol. 29, no. 8, pp. 4029–4038, Aug. 2014.
[27] B. X. Nguyen et al., "An efficiency optimization scheme for bidirectional inductive power transfer systems," *IEEE Trans. Power Electron.*, vol. 30, no. 11, pp. 6310–6319, Nov. 2015.
[28] W. Zhang and C. C. Mi, "Compensation topologies of high-power wireless power transfer systems," *IEEE Trans. Veh. Technol.*, vol. 65, no. 6, pp. 4768–4778, Jun. 2016.
[29] C. P. Steinmetz, "On the law of hysteresis," *Trans. Amer. Inst. Electr. Eng.*, vol. IX, no. 1, pp. 1–64, 1892.
[30] W. Zhong and S. Y. R. Hui, "Maximum energy efficiency operation of series-series resonant wireless power transfer systems using on-off keying modulation," *IEEE Trans. Power Electron.*, vol. 33, no. 4, pp. 3595–3603, Apr. 2018.
[31] D. E. Gaona, C. Jiang, and T. Long, "Highly efficient 11.1-kW wireless power transfer utilizing nanocrystalline ribbon cores," *IEEE Trans. Power Electron.*, vol. 36, no. 9, pp. 9955–9969, Sep. 2021.
[32] V.-B. Vu, V.-T. Phan, M. Dahidah, and V. Pickert, "Multiple output inductive charger for electric vehicles," *IEEE Trans. Power Electron.*, vol. 34, no. 8, pp. 7350–7368, Aug. 2019.
[33] S. Sun, B. Zhang, C. Rong, X. Shu, and Z. Wei, "A multireceiver wireless power transfer system using self-oscillating source composed of zero-voltage switching full-bridge inverter," *IEEE Trans. Ind. Electron.*, vol. 69, no. 3, pp. 2885–2895, Mar. 2022.

Teke Hua (Student Member, IEEE) received the B.Sc. degree in electrical engineering from Guangdong Polytechnic Normal University, Guangzhou, China, in 2019, and the M.Sc. degree in electrical engineering from Guangdong University of Technology, Guangzhou, China, in 2022. He is currently working toward the Ph.D. degree in power electronics with the Department of Electrical and Electronic Engineering, Faculty of Engineering, Hong Kong Polytechnic University, Hong Kong.

In 2022, he was with the Department of Electrical and Electronic Engineering, Faculty of Engineering, Hong Kong Polytechnic University, as a Research Assistant. His current research interests include inductive/wireless power transfer, electric vehicles and inverters.

Manxin Chen (Student Member, IEEE) received the B.Sc. degree in electronic information science and technology and the M.Eng. degree in electronic engineering from Sun Yat-Sen University, Guangzhou, China, in 2015 and 2018, respectively. He is currently working toward the Ph.D. degree in electrical engineering with the Department of Electronic Engineering, The Chinese University of Hong Kong, Hong Kong. Currently, he works as an engineer in the Hong Kong Applied Science and Technology Research Institute (ASTRI).

His research interests include power electronic converter design, PWM control, and grid-interface renewable energy applications.

Ka Wai Eric Cheng (Fellow, IEEE) received the B.Sc. degree in electrical and electronic engineering and Ph.D. degree in power electronics from the University of Bath, Bath, U.K., in 1987 and 1990, respectively. Before joining The Hong Kong Polytechnic University, Hong Kong, in 1997, he was with Lucas Aerospace, London, U.K., as a Principal Engineer. He is currently a Professor and the Director of the Power Electronics Research Centre, Department of Electrical and Electronic Engineering, Faculty of Engineering, The Hong Kong Polytechnic University.

He has authored or co-authored more than 400 articles and seven books. His research interests include all aspects of power electronics, motor drives, electromagnetic interference, electric vehicles, battery management, and energy saving.

Dr. Cheng was a recipient of the Institution of Electrical Engineers Sebastian Z De Ferranti Premium Award, in 1995; the Outstanding Consultancy Award, in 2000; the Faculty Merit Award for Best Teaching from The Hong Kong Polytechnic University, in 2003; the Faculty Engineering Industrial and Engineering Services Grant Achievement Award, in 2006; the Brussels Innova Energy Gold Medal with Mention, in 2007; the Consumer Product Design Award, in 2008; the Electric Vehicle Team Merit Award of the Faculty, in 2009; the Eco Star Award, in 2012; the Gold Prize at Seoul International Invention Fair, in 2015; the iCAN Gold Medal at Canada for contribution in active suspension, in 2016; the Gold Award of HK Innovation and Technology for contribution in body integrated supercapacitor for vehicles, in 2017, the Geneva Invention Expo Silver Medal for contribution in e-Antilock braking systems, in 2021, and TechConnect 2023 Innovation in Ammonia Electric Vehicles.